SAND2019-4294C

Response of Jointed-Structures in a Shock Tube: Simultaneous PSP and DIC with Comparison to Modeling

Kyle P. Lynch[1], Elizabeth M. Jones[2], Adam R. Brink[2], Daniel R. Roettgen[2], Robert J. Kuether[2], Justin L. Wagner[3]
Sandia National Laboratories, Albuquerque, NM 87185

Allen Mathis[4], D. Dane Quinn[5]
Akron University, Akron, OH 44325

FSI experiments are performed in a shock tube on a cylindrical structure containing internal jointed (bolted) connections. The structure is first exposed to impulsive, longitudinal forcing associated with the incident shock wave followed by transverse loading associated with vortex shedding. The aerodynamic loading is characterized with high-speed pressure sensitive paint (PSP) while digital image correlation (DIC) was used to simultaneously measure the resulting structural response. Combined analysis of the PSP and DIC data allows the amplitude and phase coupling between the transverse force and beam response to be investigated. The simultaneous aspect of the measurement is critical in identifying the relationships between loading and response for the different conditions. Further analysis with a larger data set is required to make a definitive claim on the repeatability of the experiments. Such experiments are ongoing using the methodology outlined in this extended abstract. Initial comparisons to nonlinear models using a Coulomb friction model are presented. Work is ongoing to implement and evaluate several additional reduced order models (ROMs) in ABAQUS to compare to the experiments. Ultimately, the final paper will allow the efficacy of existing jointed-structure models in complex aerodynamic environments to be evaluated.

I. Introduction

Fluid-structure interaction (FSI) in unsteady fluid dynamic environments can lead to significant uncertainties in predictions of structural response. A fair amount of FSI work has been conducted in low-speed flows e.g., [1]. Data availability in high-speed, compressible flows remains scarcer. A few examples include the structural response of a store in an aircraft bay [2], panel response under loading imposed by boundary layers [3-5], panels subjected to shock wave-boundary layer interactions [6-8] and panel response to supersonic jets. In the latter cases, attention is often given to large panel displacements (approx. panel thickness), where the structural dynamics become nonlinear [7-11].

An additional nonlinear aspect of the FSI problem involves the response of jointed structures. In comparison to their monolithic counterparts, which are appropriately modeled using linear structural dynamics, jointed structures exhibit increased energy dissipation and decreased vibrational loads [12-14]. Thus, improperly modeling joints may lead to overly conservative designs. Currently, semi-empirical constitutive models are used, based on parameters including stiffness, initiation force required for macro-slip, and energy dissipation. These can be measured by specific harmonic loading experiments using mechanical devices such as an impact hammer or a shaker table [15-17]. However, when a structure experiences a different loading environment such as a flow containing unsteady air-shocks, vortex shedding, aeroacoustics, and turbulence, it is forced in a way differently from the mechanical methods used to

[1] Senior Member of the Technical Staff, Engineering Sciences Center, Member AIAA, klynch@sandia.gov.
[2] Senior Member of the Technical Staff, Engineering Sciences Center.
[3] Principal Member of the Technical Staff, Engineering Sciences Center, Senior Member AIAA, jwagner@sandia.gov.
[4] Graduate Research Assistant, Department of Mechanical Engineering.
[5] Professor, Department of Mechanical Engineering.

calibrate the models. Ultimately, this may lead to incorrect estimates of vibrations in structures subjected to fluid-dynamic loadings.

This hypothesis motivates the present experimental campaign capable of producing and measuring the relevant fluid and structural dynamic physical phenomena present in high-speed FSI. The approach is to drive gas-phase shock waves traveling at approximately 500 m/s into canonical jointed-structures designed to exhibit a nonlinear response. Following an impulsive starting load, an unsteady wake is established in the shock-induced flow, which can be described in normalized time $t^* = tU_\infty / D$ (where U_∞ is the post-shock freestream velocity and D is the cross-sectional diameter or width of the structure). Previous high-speed particle image velocimetry (PIV) measurements in the current shock tube suggest that the impulsively started wake begins to exhibit asymmetry at $t^* \approx 5$ and reaches steady-state von Kármán vortex shedding at $t^* \approx 20$ [18, 19]. The vortex shedding exerts a transverse loading on the structure. Additionally, stochastic forcing is present due to smaller-scale turbulent fluctuations in the wake. Therefore, a physically rich fluid dynamic loading environment exists to drive the FSI, which can be used to test the fidelity of existing nonlinear structural dynamics models.

Simultaneous high-speed measurements of aerodynamic loading and structural response are required to create a model validation dataset; however, the small size of the tested structures herein (height of ≈ 13 mm) precludes the use of traditional transducers and accelerometers. Further, single-point measurements make model validation difficult because they cannot fully resolve structural mode shapes or complex pressure fields. Fortunately, high-speed, full-field alternatives are available. PSP is becoming prevalent in high-speed aerodynamics [21, 22] and DIC in high-speed FSI is gaining popularity [8, 10, 22-25].

The present work uses high-speed PSP and DIC simultaneously by placing the DIC speckle pattern overlaid on PSP. This presents challenges as aero-optical distortions associated with shock waves, turbulence, and shock-heated gas contribute to measurement noise. Additionally, since the DIC speckle is overlaid on the PSP, the DIC pattern must be filtered out to properly post-process the PSP data. Finally, high-precision DIC is required to capture the structural displacements that are as small as 5 microns. Methods to address these challenges, such as signal filtering via proper orthogonal decomposition (POD) have been described previously by Lynch et al. [26] and are incorporated in the current experimental analysis. The shock tube data are obtained at a variety of flow conditions including cases where the frequency of the jointed-beam is near the vortex shedding frequency (i.e., the "lock-in" condition [1]), as well as instances where the frequencies are not matched. This high-fidelity dataset is then used to evaluate models incorporating nonlinear energy dissipation at the joints.

The structural response of the beam is simulated using one-way-coupled structural dynamics, where the aerodynamic loading obtained via the PSP is used directly as the forcing input. The predicted response is compared to the experimental data to assess the viability of several constitutive models including Coulomb and Stribek friction [27, 28]. Additionally, more advanced models utilizing Jenkins [14] and Iwan [16] elements are evaluated. Notably, all joint models are calibrated using separate impact hammer experiments. Importantly, this allows for the ability of *independently calibrated* nonlinear models to predict response in actual FSI environments to be determined.

II. Experimental Arrangement

A. Shock Tube Facility

Experiments are performed in the Multiphase Shock Tube (MST) at Sandia National Laboratories, described in detail in [29] and shown in Fig. 1. Briefly, the MST is a shock tube with a driver section consisting of a circular pipe 89 mm in diameter that is 2.1 m long. The driver is pressurized with air at room temperature. The driven section is a square cross-section pipe of 79 mm height and width, with a length of 5.9 m. It is filled with ambient air at room temperature and atmospheric pressure of 84.1 kPa. The test section is located approximately 4.9 m downstream of the valve, and is a specialized square section with optical access via fused silica glass windows on all sides. The top and bottom portions have solid inserts and provide the mounting points for the beam. Fused-silica windows running the length of the test section with a height of 25 mm are used to image the beam.

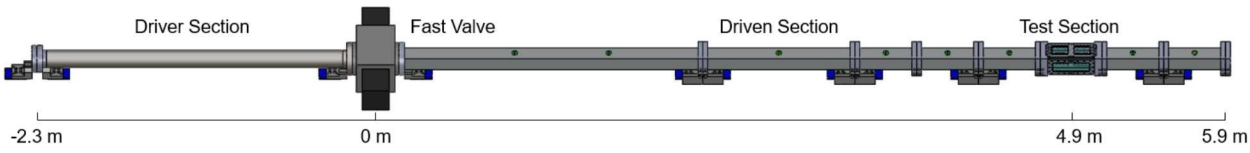

Fig. 1. Diagram of multiphase shock tube with fast-acting valve.

A Dynamics Systems Research (model 725-3.0-6000) fast acting valve acts as the diaphragm. The valve is actuated using an independent pressure source, allowing for a continuous range of driver pressure conditions. Further, the valve is electronically triggered to allow for synchronization with laser and camera equipment. The continuous range of conditions allows the strength of the structural loading to be widely varied [30].

Many conditions were used to span a range of loadings as described in Table 1. The conditions are determined by measuring the shock speed near the test section using fast-response pressure transducers, and using shock tube relations to calculate the induced velocity and Reynolds number based on beam width D. The values t_{max} and t^*_{max} are defined as the maximum test durations upon the arrival of the reflected shock. In all cases the reflected shock wave arrives prior to the driver gas contact surface. The values of f_{shed} and the associated Strouhal number St_D have been determined by the PSP in the later sections. Note that the Strouhal number is based on the initial induced velocity. However, owing to boundary layer effects [31], the velocity increases during a test by as much as ≈ 20% for the higher driver pressure conditions [30].

Table 1. Summary of test conditions.

Driver Pres. [psig]	Induced Velocity [m/s]	Shock Mach [-]	Re_D [-]	t_{max} [ms]	t^*_{max} [-]	f_{shed} [kHz]	St_D [-]
50	109	1.21	92160	5.10	43.7	1.72	0.20
75	146	1.29	131700	5.01	57.6	2.10	0.18
100	180	1.36	172500	4.93	70.3	2.58	0.18
125	191	1.39	186200	4.86	73.4	2.81	0.18
150	196	1.40	191400	4.85	74.8	3.24	0.2

B. Test Model

A simplified test specimen was designed to exhibit a nonlinear response when subjected to an impulsive loading. The model consists of a rigid back plate containing two bolted interfaces on raised flanges. These bolts connect to a flange on a thin shell as shown in Fig. 2. The pressure loading on the faces of the shell is transferred through to the bolted joint, causing a localized strain and slip that is nonlinear depending on the input loading. Further, rotation of the shell about this joint can occur under asymmetric loading imposed by vortex shedding. The pressure is measured using PSP on all three of the painted faces of Fig. 2, and DIC is measured only on the front face which is visible from both cameras.

The shell of the beam is made of 4340 alloy steel, whereas the back plate is 8630 alloy steel. The back plate of the beam is connected directly to the shock tube using ¼"-28 bolted connections, torqued to 100 in-lbs. This was verified in separate measurements to be a sufficient torque level to prevent slippage of this bolted connection during the experiment. The internal bolted connections are #3-56, torqued to 12 in-lbs. The shell piece is 0.1 in shorter than the back plate, preventing any contact between the shell and the shock tube walls as it undergoes motion.

The beam assembly is mounted in a vertical orientation within the shock tube; the resulting coordinate system is defined in Fig. 2. The origin is located on the center of the front face of the beam. Displacements in x correspond to a response generated from a front-face pressure, and y-displacements correspond to responses from asymmetric pressure loading. The z-displacements are minimal, as this is along the longitudinal axis of the beam.

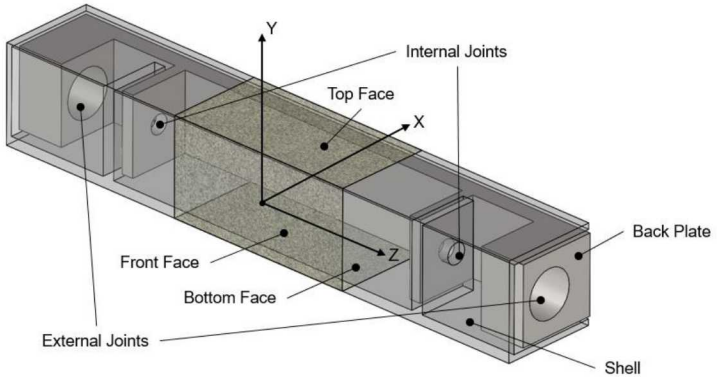

Fig. 2. Solid model of two-piece test specimen. Textured brown regions indicate PSP-coated faces.

C. Optical Setup

A stereo imaging configuration is used as shown in Fig. 3. Phantom v2512 and v2511 high speed cameras are used for imaging (28 µm pixels, 1280 x 800 px at 20 kHz). A cropped image size of 896 x 512 was used for this experiment, while the frame rate is maintained at 20 kHz to yield an exposure time of 49 µs for capturing sufficient signal from the PSP. A pair of Nikon 105 mm lenses are used with Lavision Scheimpflug mounts, allowing a low f/# = 5.6 to capture additional signal while aligning the focal plane with the front face of the beam. To our knowledge, this is the first application of Schiempflug imaging for DIC measurements. The field-of-view captured the center 25 mm of the front face of the beam in both camera systems, and the center portion of the left or right sides of the beam in the left and right camera system, respectively. In the results shown here, viewing of the entire beam length was precluded by the 25-mm tall test section windows; however, the final paper will include data with larger windows capable of capturing the entire beam length. The physical scaling of the system is 15.6 px/mm. With the low f/# (large aperture) the depth-of-field was smaller than the depth of the beam, even with the Schiempflug mounts; therefore, as a compromise between the DIC on the front surface and the PSP on the top/bottom faces of the beam, the focus plane was set slightly behind the front face of the beam, so that the sides of the beam were also within the depth-of-field. The cameras were mounted on a set of optical rails to adjust the stereo angle and working distance. The stereo-angle, defined as the total angle between the lenses, was approximately 60º, and the stand-off distance was approximately 200 mm. These were further mounted to a large floating vibration isolation table to eliminate propagation of shock tube motion through to the cameras. The resulting stability of the system eliminated the need for shot-to-shot camera calibrations.

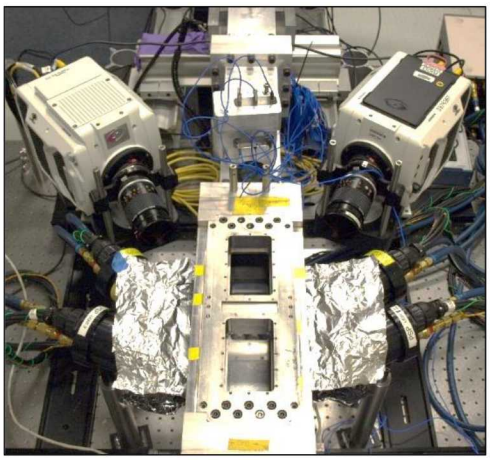

Fig. 3. Photo of optical setup.

D. Pressure Sensitive Paint

The PSP implementation uses a formulation recently proposed by [32]. A ruthenium luminiphore ($Ru(dpp)_3$) is mixed within a silicone rubber (RTV) binder containing nanoscale boron nitride particles. The particles provide a porous surface for interaction with surrounding oxygen, yielding a time response of approximately 12 µs. The three constituents are mixed following an 80% particle-to-(polymer+particle) weight ratio using toluene as a solvent:

$Ru(dpp)_3$: polymer : particle : toluene = 3 mg : 60 mg : 240 mg : 10mL

The formulation was well-stirred for two hours using a magnetic stirrer and applied using an airspray gun. The paint cured for four hours in a vacuum chamber. Unlike sprayable fast-PSP based on platinum-tetra-fluoro-phenyl-porphrin (PtTFPP) requiring a two-part application procedure, this paint is applied in one step.

Illumination is provided by two ISSI LM2XX-DM-400 and two ISSI LM2XX-DM-460 water-cooled LED arrays, each outputting between 8-12 W at 400 ± 17 and 460 ± 31 nm, respectively. The light enters the test section via the same side windows used for imaging and additionally using ceiling and floor windows. The LED arrays are placed as near to the model as possible to maximize incident light. The paint excitation wavelength peaks at 475 nm, and emits at a center wavelength of 600 nm, allowing a 590 nm long-pass filter to remove excitation light.

The Stern-Volmer ratiometric method is used to convert image intensities to pressures (see e.g. [33]). The in-situ calibration of [32] found a pressure sensitivity of 0.62%/kPa and temperature sensitivity of 1.05%/ºC for this formulation. This temperature sensitivity is significantly less than PtTFPP, which is particularly advantageous for use in a shock tube where there is a temperature rise after the shock. Unfortunately, the test section design in the current tests precluded an in-situ calibration, so an alternative conversion was applied as follows. The 'wind-off' image I_0 is compiled from the average of 10 acquired images before the arrival of the shock wave, and the ratio I_0/I is compiled for each subsequent image. An initial intensity ratio $(I_0/I)_0$ is calculated from an average of 10 ratios before the incident shock arrives. A final intensity ratio $(I_0/I)_R$ is calculated after the arrival of the reflected shock. The signal is then normalized by these values and multiplied by the pressure after the reflected shock p_R as measured using an external sensor such that pressure p is calculated as follows:

$$p = \frac{p_R(I_0/I)}{(I_0/I)_R - (I_0/I)_0} \tag{1}$$

This effectively corresponds to a linear calibration curve between the initial pressure and post-reflected shock pressure. For the present experiment the focus is on the frequency content of the pressure fluctuations rather than the absolute calibrated pressure values, and therefore this linear assumption is accepted. The local flow velocity after the reflected shock is approximately stationary, therefore the pressures on all faces of the beam and sidewalls of the shock tube should be identical, justifying the above scaling.

An image registration procedure is required when analyzing PSP to map the images to a physical coordinate system. Furthermore, during a run the beam vibrates and will cause the 'wind-on' images to lose alignment with the reference. This issue is common in wind tunnel facilities and can be corrected using image registration with multiple-markers [35, 36], or lifetime PSP which does not require a wind-off reference [37]. The former is applied in this work. A three-step procedure is therefore used to process the images.

The first step applies a projective transformation to 'unwrap' the images from the sides and front of the beam to the known physical coordinates of the beam. The projective transform is defined from four points manually identified on each face in the reference image. This is a simplified version of the more generic image registration approach using photogrammetry of multiple targets, and is applicable here since planar surfaces are being investigated and because an image alignment procedure is used as discussed below. Examples of raw and unwrapped images is shown in Fig. 4.

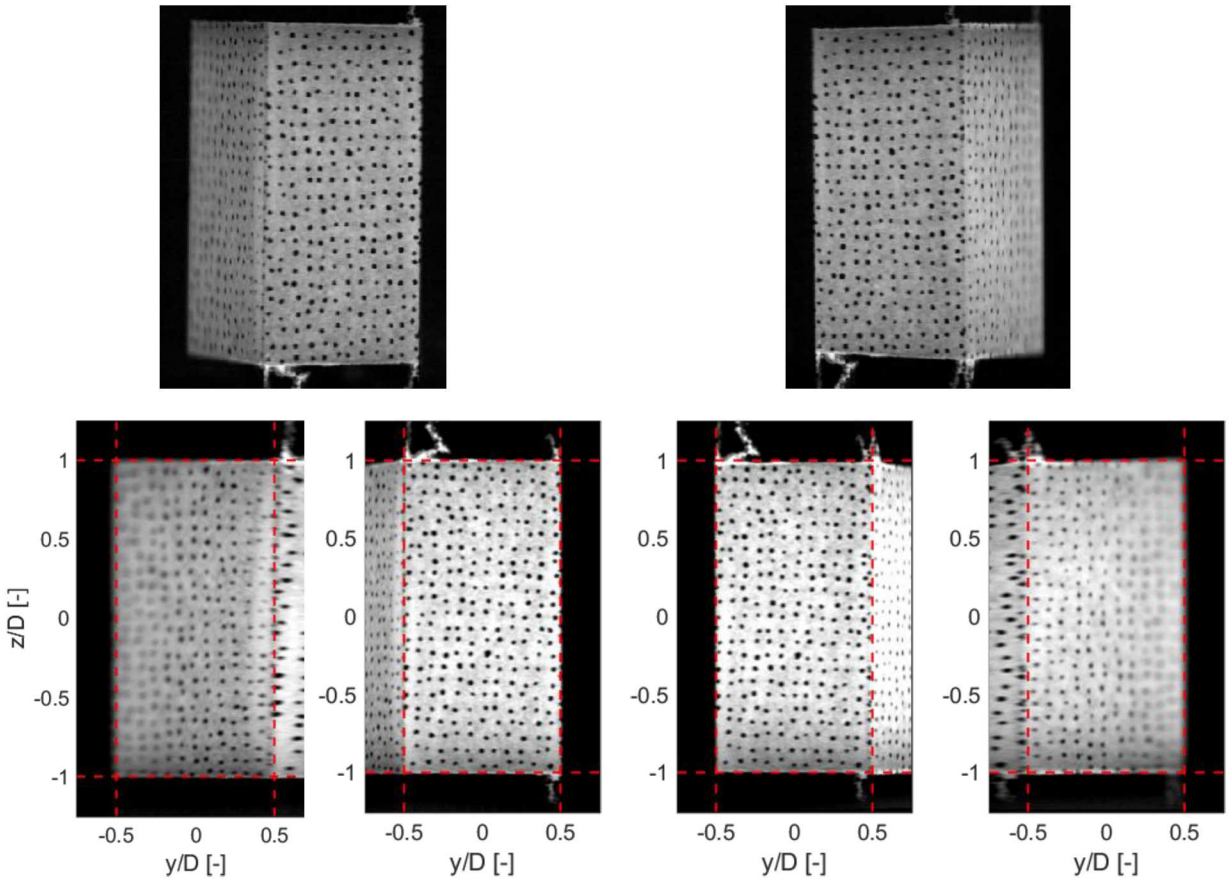

Fig. 4. Top row, example raw PSP images from left and right cameras. Bottom row, dewarped images.

The second step corrects for small misalignments due to vibrations. The speckle pattern on all sides of the beam is exploited to allow a rigid image registration algorithm to be used for the alignment (Matlab imregister). Each image of each face is independently registered to its corresponding reference image before taking the intensity ratio. Also, since the front face of the beam is seen by both cameras, the registered faces can be averaged to reduce image noise along this face. An example of intensity ratios with and without the registration are shown in Fig. 5. In the unregistered ratio, the misalignment between the speckle pattern leads to division by low intensity values and residual spikes in

intensity near speckles. In the registered ratio, there is little evidence of intensity spikes near speckles, indicating a successful alignment to within a pixel.

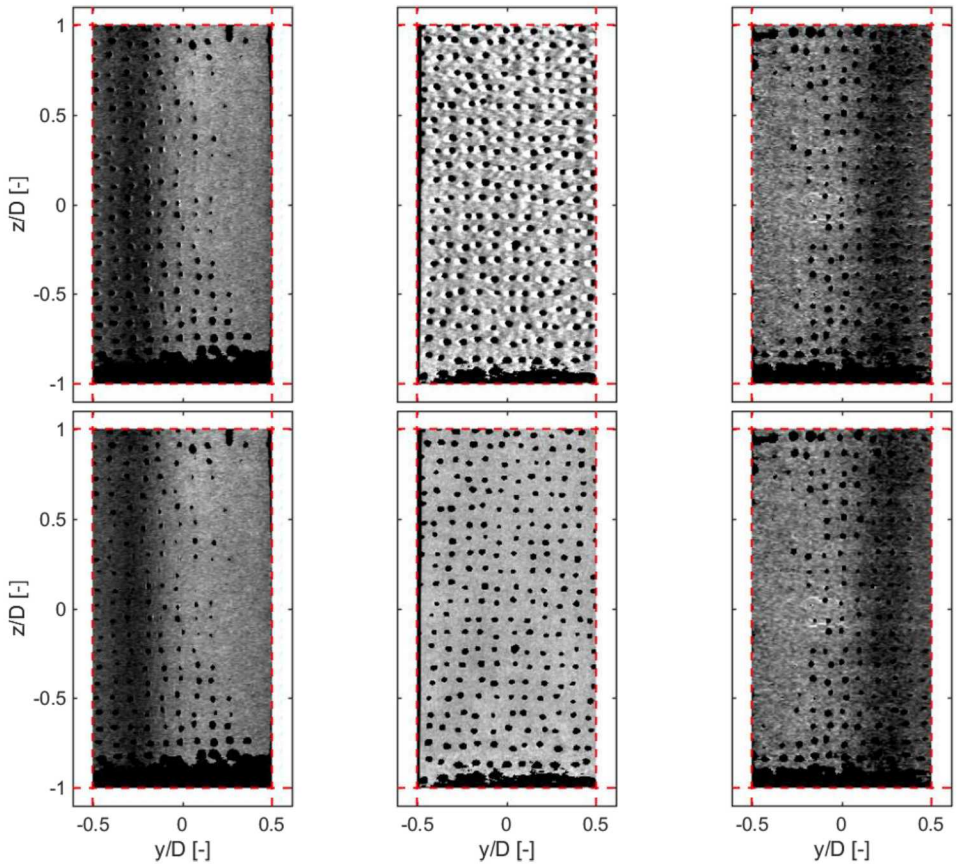

Fig. 5. Top row, unregistered ratio for all faces of the beam. Bottom row, registered intensity ratio. Timestep corresponds to arrival of incident shock.

The last step is to separate the speckle pattern from the PSP signal, and if desired, fill in the speckle pattern. A simple threshold of 30% of the mean reference image intensity is used to create a mask. Following this, the masked regions are filled using a Laplacian inpainting algorithm (Matlab regionfill). An example of the masking, filling, and front-face averaging operations is given in Fig. 6.

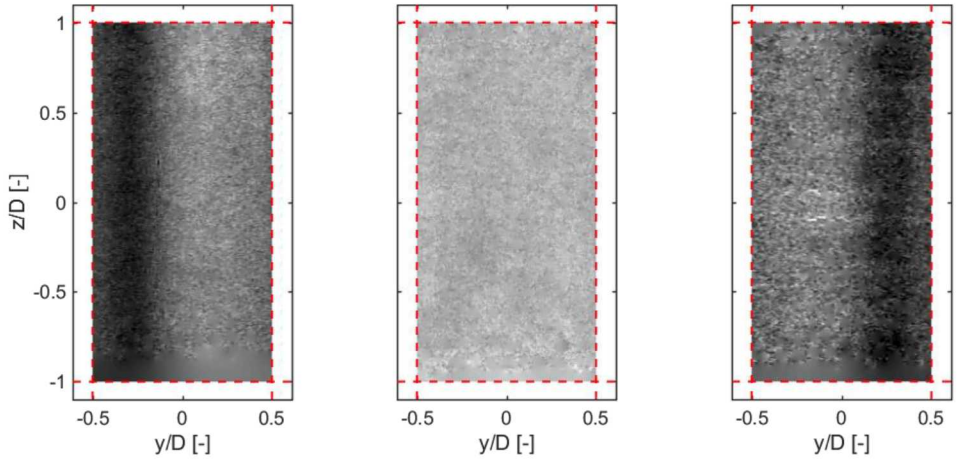

Fig. 6. Example filled ratios. Timestep corresponds to arrival of incident shock.

E. Digital image correlation

Stereo DIC is used to measure the surface deformation of the front face of the beam; this is the only side that is seen by both cameras. The speckle pattern was applied on all sides using a simple ink stamp (Correlated Solutions square ink stamp, 0.013 mm dot size). As discussed above, the speckle pattern on the sides used only for the PSP image registration and not DIC. The thin layer of ink effectively blocks the UV excitation light from reaching the lumiphores and results in a high-contrast pattern. A sparse speckle pattern was used as a compromise between the optimal speckle density for DIC and maintaining sufficient PSP paint uncovered. In 16-bit quantization, the minimum intensity within the speckles is around 1900 counts, the maximum intensity is around 14000 counts, and the image noise level, defined here as standard deviation of the background, is 260 counts. This yields a contrast, defined here as (14000-1900) / 260 = 50, which was found to be sufficient for DIC processing.

Correlated Solutions VIC-3D v8 software was used for calibration and evaluation. Two sets of calibration images were collected, one using a standard dot-grid calibration target and a second using a speckled flat plate that filled the field of view. Approximately 100-200 images were captured of each target as the target was rotated, tilted, and plunged within the field-of-view and depth-of-field of the two optical systems. First, a standard calibration was performed, using only the images of the dot-grid target and a radial, 3rd order camera model. Because of the thick windows and glancing angle of the cameras with respect to the windows, this calibration process was unable to adequately model the stereo-system, and the profile of the beam in static conditions reconstructed with the DIC data was distorted by approximately 100 microns. Correlated Solutions recently introduced a complex camera model (variable ray origin; VRO, 5th order), which takes tangential distortions into account. However, calibrating this complex model using only the dot-grid calibration target again produced a distorted beam profile. This is caused by (1) low precision in the algorithms to extract the location of the dots and (2) insufficient number of calibration points in 3D space. To address these issues, a hybrid calibration was used. This method used the correlation results from the speckled plate to calibrate the complex camera model, and only used the dot-grid target to set the scale (pixels to millimeters). With the hybrid calibration, the profile of the beam surface is much more realistic, with an order of magnitude lower error in beam shape estimation. This hybrid calibration process was successfully used both with and without the Schiempflug mounts.

Processing used a subset size of 35 pixels, a step size of 10 pixels, and an affine subset shape function. Because the beam motion during the experiment had low spatial gradients, a large subset size was used to reduce noise, and a large step size was used to reduce processing time over 6000 images. To account for the variation in image intensity between the reference and 'wind-on' images, it was required to use a zero-mean normalized cross-correlation. A low-pass filter was applied to the images prior to correlation.

As detailed by Lynch et al. [26], a high-pass filter is applied to the DIC data to remove large-scale motion/recoil of the shock tube. The filter is a 4-pole Butterworth filter with a cutoff frequency of 500 Hz and stopband attenuation of 80 dB. Finally, independent tests using a rigid beam were used to estimate the measurement uncertainty. These experiments yielded random and bias errors of approximately +/- 3 microns in v and +/- 8 microns in u after the passage of the shock. At the time of shock passage, the errors rise to +/- 5 microns in v and +/- 40 microns in u owing to refraction [26].

III. Initial Results

A. Pressure Sensitive Paint

The PSP results are verified by comparison to fast-response pressure transducers (PCB Piezoelectronics 113B27, 100 psi range) located on the wall near the beam location. The comparison is not valid after the incident shock, as the pressure field around the beam will cause a locally increased pressure near the front face (stagnation region), and decreased pressure around the side faces (separated flow). However, after the reflected shock the flow is approximately stagnant, and the pressures on all faces and on the wall transducer should be the same.

An example 75 psi run is shown in Fig. 7, showing pressure averaged over the entire faces of the beam and the wall-mounted PCB result. Note that the PCB signal has been aligned in time with the arrival of the incident shock, even though it is at a further downstream location than the beam. This causes the reflected shock to arrive earlier in time for the beam signal; however, this does not change the comparison, as the pressure value is essentially identical for transducers located before or after the beam.

Following the incident shock, the pressure rapidly rises on all sides of the beam, with a loading on the front approximately twice that of the side. The pressures on the sides of the beam exhibit an in-phase shedding initially, then transition to an out-of-phase shedding for the remainder of the run. This transition occurs at around t = 1.2-1.5 milliseconds, corresponding to a t* = 16-20. This is consistent with the time for complete transition from asymmetric

to symmetric wake shedding as reported in the high-speed PIV measurements of [19]. This is further pronounced in the integrated transverse force shown in Fig. 7. The pressure is assumed to be approximately constant along the span, therefore the pressure measurement on the central portion is used to calculate the force on the entire beam.

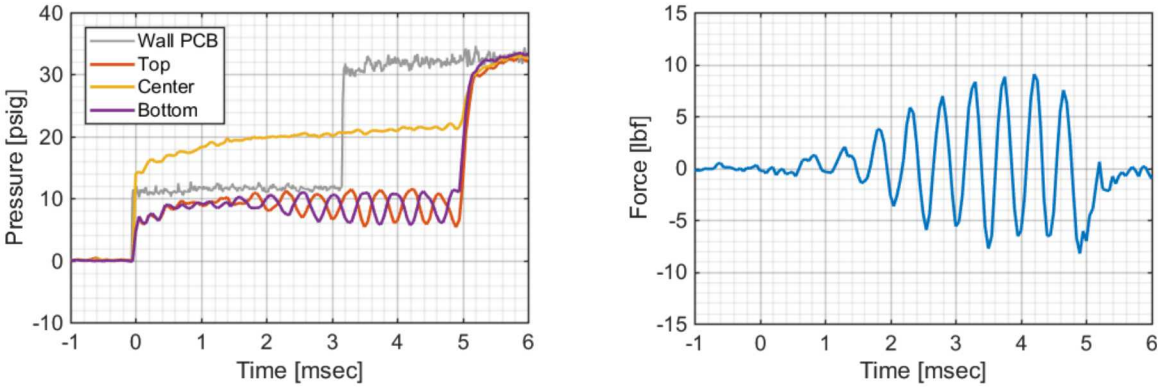

Fig. 7. Left, comparison of spatially-averaged pressure traces from PSP and wall-mounted PCB sensor for a 75 psi driver condition. PSP signal averaged over entire faces. Right, integrated transverse force from pressure data.

A clear periodic forcing is observed after the transition to asymmetric shedding. In figure 8, the analysis is extended to all conditions. Example traces of the integrated force are shown on the left. An increase in forcing frequency is visible as the pressure is increased, with a dramatic increase in forcing amplitude at the 75-psi condition. The power spectral density of these traces, normalized by their respective sums, is shown on the right. A clear trend is visible: as the driver pressure, and equivalently Reynolds number and flow velocity, increases, the forcing frequency increases. This is consistent with a constant Strouhal number of approximately 0.2 for an increasing induced velocity after the shock.

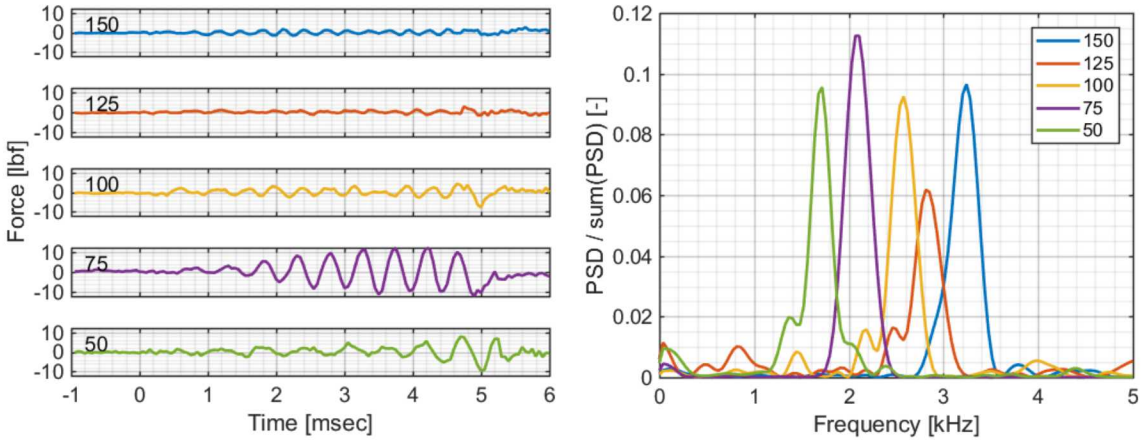

Fig. 8. Power spectral density of transverse force loading as a function of driver pressure (see Table 1 for corresponding Reynolds number).

B. Digital Image Correlation

Displacement results for an experiment with a driver pressure of 150 psi are shown in Fig. 9. Immediately apparent is a strong oscillatory behavior in the v-component that occupies a varying envelope. There is also less-pronounced periodic motion in the u-component. The oscillations occur in both the u- and v-component of displacement (the w-component is approximately zero), suggesting a motion that is coupled in these two coordinate directions. This is the case for rocking, which is manifested as a coupled u-v motion. However, the nature of the motion is difficult to distinguish just by inspection of the u-w displacements.

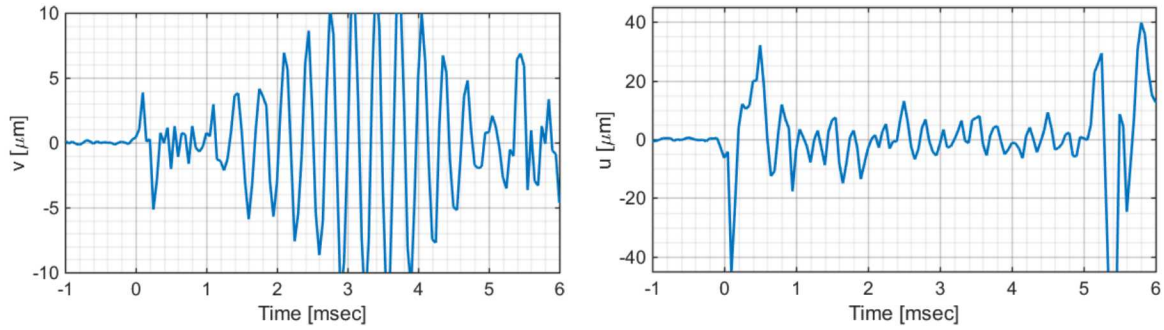

Fig. 9. Example displacement signals for 150-psi case after application of spectral filter.

An alternative approach is to apply proper orthogonal decomposition (POD) to decompose the displacement data $\boldsymbol{u}(\boldsymbol{x},t)$ into a set of spatially-dependent modes $\boldsymbol{\phi}_i(\boldsymbol{x})$ and time-dependent mode coefficients $a_i(t)$ according to equation 2, where $\boldsymbol{x}$ are the set of spatial coordinates, t is the time, i is the mode index, and the overbar indicates a time-average. Following the procedure in [37], the u-, v-, and w- components are formatted into a single matrix, and the Matlab 'pca' function is used to perform the decomposition.

$$\boldsymbol{u}(\boldsymbol{x},t) - \overline{\boldsymbol{u}}(\boldsymbol{x}) = \sum_{\boldsymbol{i}} a_i(t)\boldsymbol{\phi}_i(\boldsymbol{x}) \tag{2}$$

The mode shapes $\boldsymbol{\phi}_i(\boldsymbol{x})$ provide a clearer picture of the underlying beam motion rather than direct inspection of the displacement fields. The first three modes are shown in Fig. 10. The modes are multiplied by a mode coefficient of -1/+1 (red/blue) to assist visualization of their oscillatory behavior. Mode 1 represents a u-displacement toward and away from the beam, consistent with the constant offset previously noted because of shock wave passages. This can also represent any in-plane offsets caused by other sources of aero-optic distortion or actual motion of the beam. Mode 2 is a rocking mode, where the face of the beam rotates along its central axis and causes a coupled v- and u-displacement. Mode 3 is an additional rocking mode.

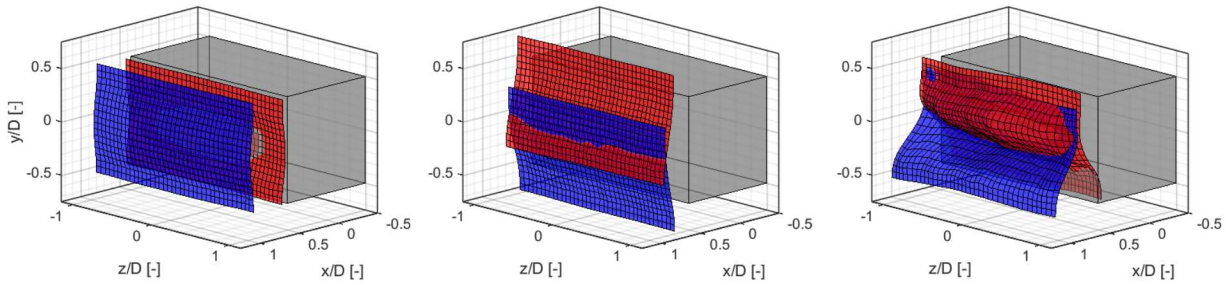

Fig. 10. Left to right: POD modes 1, 2, and 3 of beam displacement. Red and blue represent the mode shapes multiplied by -1 and +1 mode coefficients a_i.

The relevance of these and further modes is examined by the cumulative mode energy distribution in Fig. 11. For the 150-psi case the first two modes are responsible for 62% and 10% of the variance, respectively, with the remaining modes contributing less than 1% of the variance. This residual variance captured in the higher modes is attributed to the measured small-scale aero-optic distortions. The lower pressure cases exhibit slower modal convergence, possible due to the lower magnitude of the beam motion over the sources of noise.

The mode coefficients $a_i(t)$ are time-dependent; plotting their time-series illustrates when the 'offset' or 'rocking' modes are active during the run. These are shown in Fig. 11 together with the time-of-arrival of the incident and reflected shocks. Activity in mode 1 is immediate upon arrival of both shocks, indicating that the 'offset' mode is activated either by force due to the shock loading, or due to aero-optic distortion. In contrast, the 'rocking' mode 2 takes time to establish after the shock, which is consistent with the required time for the onset of vortex shedding in the impulsive flow. Mode 3 is drastically lower in modal coefficient amplitude, consistent with the low explained variance by this mode; no clear evidence of oscillations in this mode is observed.

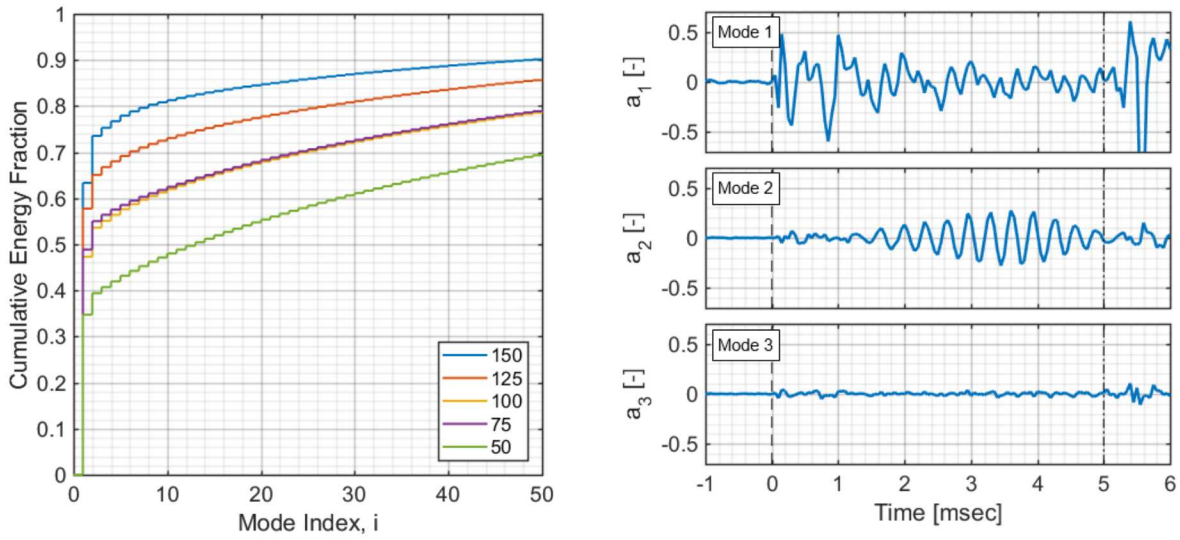

Fig. 11. Left, cumulative mode energy distribution for multiple cases. Right, time-dependent mode coefficient plot for modes 1 through 3 for a 150-psi case. Long dashed/dashed-dotted lines indicate incident and reflected shock arrival times, respectively.

C. Combined Analysis

Attention now turns to the combined analysis of the PSP and DIC data to identify the relation between loading and the response. Examples of combined signals are shown in Fig. 12; the frontal force from the PSP is also shown to clearly identify the moment of shock impingement on the model. Note that the signals have been normalized by their respective RMS values over the duration of the test to place them with a similar scale.

The 75-psi case stands out immediately as having a nearly exact phase and frequency match between the PSP and DIC signals; the signals appear to be 'locked-in' to each other. The two signals grow after a delay of approximately 1.5 milliseconds, reaching their maximum amplitude right before the arrival of the reflected shock. After the reflected shock, both the pressure loading and response quickly decline. Another notable case is at 150 psi, where the frequency appears to be similar, but exhibits a phase mismatch between the PSP and DIC signals.

To quantitatively describe the relationships between these signals, the cross-power spectral density (CPSD) can be used to supplement the individual PSDs of the PSP and DIC signals. Briefly, the CPSD is a complex quantity, whose magnitude describes the degree of cross-correlation at each frequency, and whose complex angle represents the phase shift between signals. Overlays of the PSDs, CPSDs, and CPSD angles for various cases are shown in Fig. 13. In all cases, the PSD/CPSD amplitudes are normalized by their sum for comparison.

A surprising bi-modal behavior is observed in Fig. 13 as the driver pressure is increased. For the 50 and 75 psi cases, the DIC mode 2 has a frequency component at the lower frequency of around 2.0 kHz; for the 50-psi case, the primary mode component is also observed at 3.0 kHz. For 75 psi however, both the PSP and DIC signals show nearly exact amplitude content at the lower 2.0 kHz frequency. Examining the angles, it appears in these two cases the DIC signal *leads* the PSP signal by a small phase shift. This is clearly visible for the 75-psi case in particular by examining the previous Fig. 12. This suggests that the beam itself may be influencing the vortex shedding, indicating a two-way coupled problem. If this is in fact the case, one-way-coupled structural dynamics simulations will clearly fail.

For the 100-150 psi cases, the nominal vortex shedding frequency has increased above 2.0 kHz, and the DIC response shifts toward the natural frequency at 3.0 kHz. The signals at 100 and 125 psi have very low phase angles, indicating the pressure signal is nearly exactly matched in phase with the DIC signal. Again, cursory inspection of Fig. 12 confirms this; however, the amplitude match in Fig. 12 appears to be erratic. Finally, at 150 psi, the vortex shedding frequency appears to be slightly higher than the beam natural frequency, and the angle shows the shedding loading to precede the DIC response. This is confirmed in Fig. 12, where the initial 1-2 periods appear to be closely matched, after which the pressure signal exhibits a higher frequency than the DIC signal, and thus produces a phase shift throughout the duration of the run.

The preceding analysis is performed using data from only a single run at each condition, therefore the repeatability needs to be checked by conducting additional runs before drawing strong conclusions on beam and flow dynamics. Nevertheless, the combined analysis demonstrates the importance of the simultaneous diagnostics shown herein.

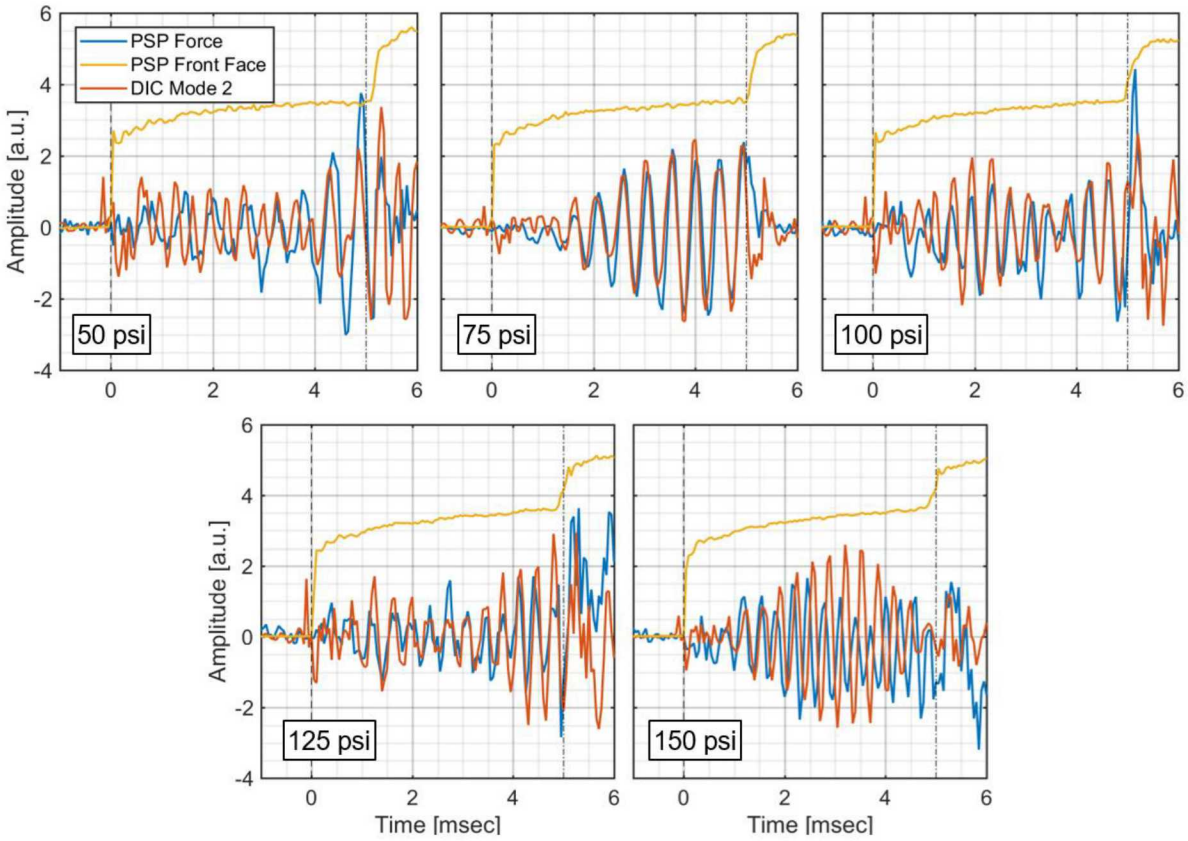

Fig. 12. Combined time traces of PSP force and DIC mode 2 coefficients for range of pressures. Dashed lines indicate incident and reflected shock times, respectively.

D. Modeling Comparison

Finite element modeling is employed using the finite element analysis (FEA) solver ABAQUS. Comparisons of experimental data obtained during a 150-psi experiment to that predicted using the Coulomb solver available in ABAQUS are shown in Fig. 14. The simulated joint torque is set to 12 in-lbs as in the experiment and the coefficient of friction is set to 0.3. Although not shown here, movies from the simulation show encouraging qualitative comparisons to the experiment. Namely, the u-displacement (mode 1) and rocking motion (mode 2) were observed in the simulation. On the other hand, there are some significant discrepancies between the modeling and the experiment. For instance, the simulation tracks the pressure loading closely, whereas the experiment suggests a growth in rocking motion to occur even as the pressure loading decays. Naturally, it is difficult to draw conclusions from the single comparison shown in Fig. 14. As detailed subsequently, the final paper will include experimental uncertainties and comparisons to several constitutive models incorporating joint nonlinearities.

IV. Planned Results for Aviation 2019

A. Ongoing Experiments

The previous experimental results consisted of only a single run at each condition. With the experimental techniques developed by Lynch et al. [26], it is now possible to efficiently perform many shock tube experiments at each condition to quantify measurement uncertainties. These experiments are ongoing and are taking advantage of larger shock tube windows allowing for the entire beam to be measured. The larger windows also allow more light to enter the test section to improve the signal-to-noise of both the PSP and DIC.

B. Ongoing Modeling

Several nonlinear joint models are to be evaluated in ABAQUS including those assuming Stribek friction [27, 28]. and those utilizing Jenkins [14] and Iwan [16] elements. Unlike the Coulomb model, these additional models are not available and require custom implementation into the FEA solver, which is ongoing. The parameters for these models are determined using separate benchtop experiments involving DIC on the beam subjected to an impact hammer. Details on this calibration process and FEA implementation will be included in the final paper.

The final paper will use the detailed experiments to evaluate how well existing jointed-structures models perform under complex FSI environments.

Conclusions

FSI experiments have been performed in a shock tube on a cylindrical structure containing internal jointed (bolted) connections. The structure was first exposed to an impulsive, longitudinal force associated with the incident shock wave followed by transverse loading associated with vortex shedding. The aerodynamic loading was characterized with high-speed PSP while DIC was used concurrently to measure the resulting structural response. Combined analysis of the PSP and DIC data allowed the amplitude and phase coupling between the transverse force and beam response to be investigated. The simultaneous aspect of the measurement was critical in identifying the relationships between loading and response for the different conditions. Further analysis with a larger data set is required to make a definitive claim on the repeatability of the experiments. Such experiments are ongoing using the methodology outlined in this abstract.

Initial comparisons to nonlinear models implemented in ABAQUS using a Coulomb friction model were presented. Work is ongoing to implement and evaluate several additional ROMs to compare to the experiments. Ultimately, the final paper will allow the efficacy of existing jointed-structure models to predict complex FSI loading to be evaluated. To the knowledge of the authors, such an extensive comparison would be the first of its kind.

Acknowledgements

Seth Spitzer and Paul Farias are kindly acknowledged for their extensive support in model preparation including application of the PSP and machining. Tom Grasser is thanked for his help with the experimental model design.

Sandia National Laboratories is a multimission laboratory managed and operated by National Technology & Engineering Solutions of Sandia, LLC, a wholly owned subsidiary of Honeywell International Inc., for the U.S. Department of Energy's National Nuclear Security Administration under contract DE-NA0003525. This paper describes objective technical results and analysis. Any subjective views or opinions that might be expressed in the paper do not necessarily represent the views of the U.S. Department of Energy or the United States Government.

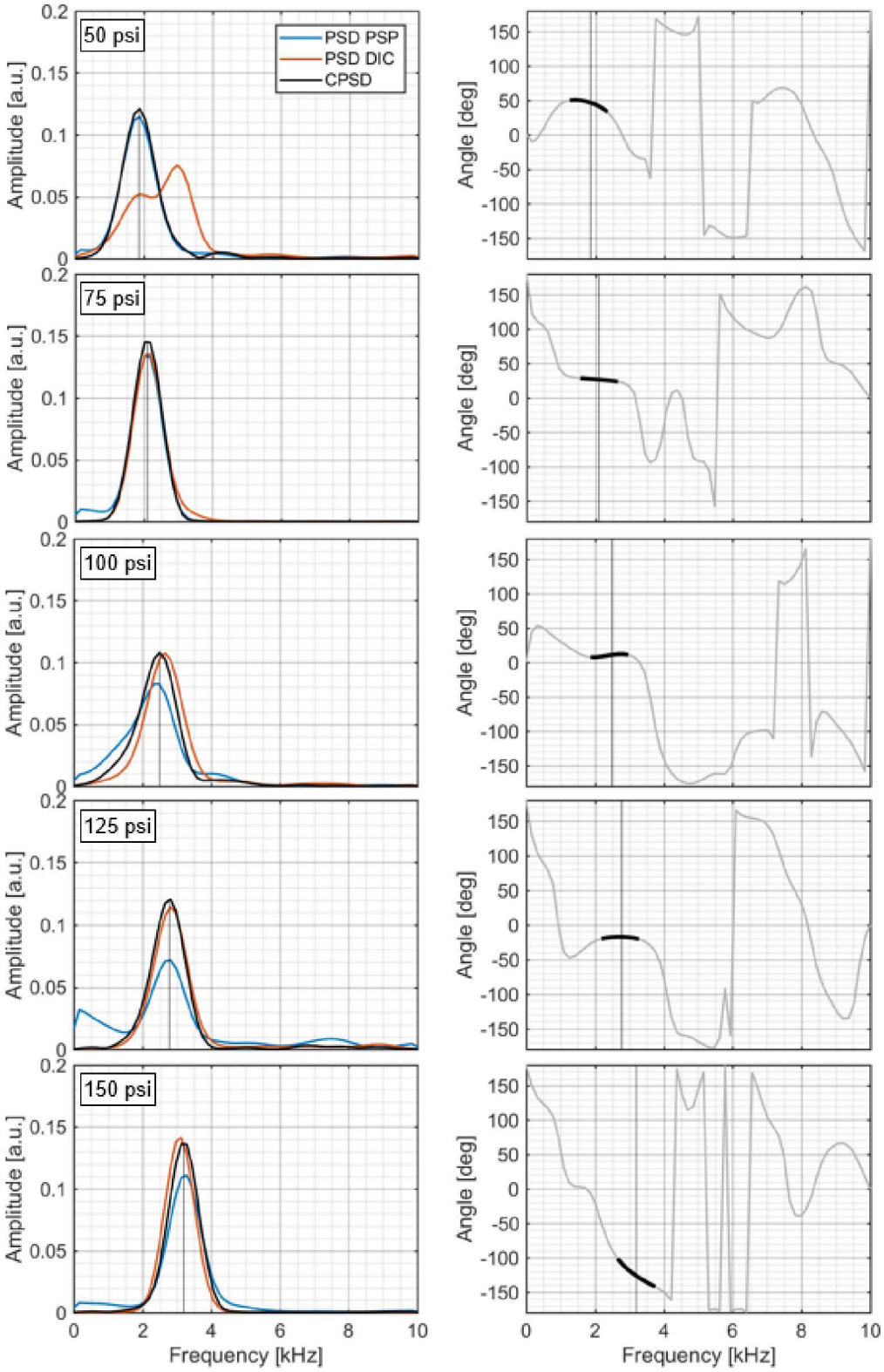

Fig. 13. PSD and CPSD comparisons of multiple cases. Left, overlays of PSD and CPSD amplitudes, normalized by respective sums. Right, CPSD angle. Highlighted angle and vertical dashed lines represents region/location of peak CPSD amplitude.

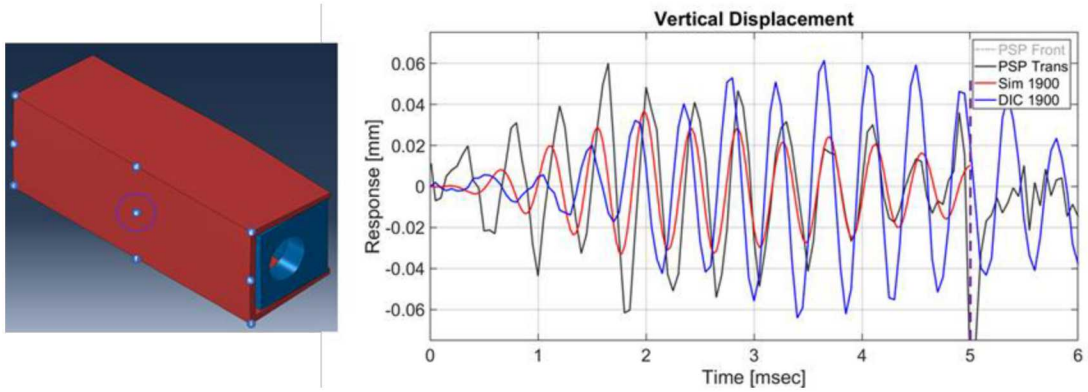

Fig. 14. Comparison of experimental data to nonlinear FEA modeling incorporating Coulomb friction. Left, test structure including the deflected shell (red) and backplate (blue) rendered in ABAQUS. Right, vertical forces as determined by PSP (black), measured vertical displacement (blue) and simulated displacement (red). The displacement locations are at the center of the front face as circled in the left figure. The dashed line corresponds to the arrival of the reflected shock.

References

[1] Sarpkaya, T., "A Critical Review of the Intrinsic Nature of Vortex-Induced Vibrations," *Journal of Fluids and Structures*, Vol. 19, No. 4, 2004, pp. 389-447.

[2] Wagner, J. L., Casper, K. M., Beresh, S. J., Hunter, P. S., Spillers, R. W., and Henfling, J. F., "Response of a Store with Tunable Natural Frequencies in Compressible Cavity Flow," *AIAA Journal*, Vol. 54, No. 8, 2016, pp. 2351-2360.

[3] Blackman, D. R., Clark, D. M., McNulty, G. J., and Wilby, J. F., "Boundary Layer Pressure Fluctuations and Structural Response, Technical Report AFFDL-TR-67-97, Air Force Flight Dynamics Laboratory, October 1967.

[4] Casper, K. M., Beresh, S. J., Henfling, J. F., Spillers, R. W., Hunter, P. S., and Spitzer, S M., "Hypersonic Fluid-Structure Interactions on a Slender Cone," AIAA Paper 2018-1825, January 2018.

[5] Currao, G., Neely, A. J., Buttsworth, D. R., and Choudhury, R., "Measurement and Simulation of Hypersonic Fluid-Structural Interaction on a Cantilevered Plate in a Mach 6 Flow, AIAA Paper 2016-1088, January 2016.

[6] Maestrello, L., and Linden, T. L. J., "Measurements of the response of a panel excited by shock boundary-layer interaction," *Journal of Sound and Vibration*, Vol. 16, No. 3, 1971, pp. 385-391.

[7] Willems, S., Gülhan, A., and Esser, B., "Shock induced fluid-structure interaction on a flexible wall in supersonic turbulent flow," *Progress in Flight Physics*, Vol. 5, 2013, pp. 285-308.

[8] Perez, R., Bartram, G., Beberniss, T., Wiebe, R., and Spottswood, S. M., "Calibration of Aero-Structural Reduced Order Models Using Full-Field Experimental Measurements," *Mechanical Systems and Signal Processing*, Vol. 86, 2017, pp.49-65.

[9] Maestrello, L., "Control of Shock Loading from a Jet in a Flexible Structure's Presence," *AIAA journal*, vol. 38, no. 6, 2000, pp. 972-977.

[10] Hortensius, R., Dutton, J. C., and Elliott, G. S., "Simultaneous Planar PIV and sDIC Measurements of an Axisymmetric Jet Flowing Across a Compliant Surface," AIAA Paper 2017-1886, January 2017.

[11] Dowell, E. H., "Panel Flutter-A Review of the Aeroelastic Stability of Plates and Shells," *AIAA Journal*, Vol. 8, No. 3, 1970, pp. 385-399.

[12] Gaul, L., and Lenz, J., "Nonlinear Dynamics of Structures Assembled by Bolted Joints," *Acta Mechanica*, Vol. 125, No. 1-4, 1997, pp. 169-181.

[13] Gaul, L., and Nitsche, R., "The Role of Friction in Mechanical Joints," *Applied Mechanics Reviews*, Vol. 54, No. 2, 1991, pp. 93-106.

[14] Brake, M.R., "An Overview of Constitutive Models," In *The Mechanics of Jointed Structures*, Springer, Cham, 2018, pp. 207-221.

[15] Segalman, D. J., "A Four-Parameter Iwan Model for Lap-Type Joints, *Journal of Applied Mechanics*, Vol. 72, No. 5, 2005, pp. 752-760.

[16] Iwan, W. D., "A Distributed-Element Model for Hysteresis and its Steady-State Dynamic Response," *Journal of Applied Mechanics*, Vol. 33, No. 4, 1966, pp. 893-900.

[17] De Wit, C. C., Olsson, H., Astrom, K. J., and Lischinsky, P., "A New Model for Control of Systems with Friction," *IEEE Transactions on Automatic Control*, Vol. 40, No. 3, 1995, pp. 419-425.

[18] Lynch, K. P. and Wagner, J. L., Time-Resolved Pulse-Burst Tomographic PIV of Impulsively-Started Cylinder Wakes in a Shock Tube, AIAA Paper 2018-2038.

[19] Wagner, J. L., DeMauro, E. P., Casper, K. M., Beresh, Lynch, K. P., and Pruett, B. O., "Pulse-Burst PIV of an Impulsively Started Cylinder in a Shock Tube for Re > 10^5," under review in *Experiments in Fluids*, 2018.

[20] Liu, T., Burner, A. W., Jones, T. W. and Barrows, D. A., "Photogrammetric Techniques for Aerospace Applications," *Progress in Aerospace Sciences*, Vol. 54, 2012, pp.1-58.
[21] Flaherty, W., Reedy, T. M., Elliott, G. S., Austin, J. M., Schmit, R. F. and Crafton, J., "Investigation of Cavity Flow using Fast-Response Pressure-Sensitive Paint," *AIAA Journal*, Vol. 52, No. 11, 2012, pp.2462-2470.
[22] Sellers, M., Nelson, M. and Crafton, J. W., "Dynamic Pressure-Sensitive Paint Demonstration in AEDC Propulsion Wind Tunnel 16T," AIAA Paper 2016-1146, January 2016.
[23] Beberniss, T. J., Spottswood, S. M., Erhhardt, D. A., and Perez, R., "Nonlinear Response of a Thin Panel Subjected to a Shockwave Impingement and Thermal Buckling, AIAA Paper 2017-3555, June 2017.
[24] Spottswood, S.M., Eason, T., and Beberniss, T., "Full-field, Dynamic Pressure and Displacement Measurements of a Panel Excited by Shock Boundary Layer Interaction, AIAA Paper 2013-2016, May 2016.
[25] Ogg, D. R., Rice, B. E., Peltier, S. J., Staines, J. T., Claucherty, S. L. and Combs, C. S., "Simultaneous Stereo Digital Image Correlation and Pressure-Sensitive Paint Measurements of a Compliant Panel in a Mach 2 Wind Tunnel," AIAA Paper 2018-3869, June 2018.
[26] Lynch, K. P., Jones, E. M., and Wagner, J. L., "Simultaneous PSP and Surface Deformation Measurements for Fluid-Structure Interactions in a Shock Tube," AIAA Paper 2018-3870, June 2018.
[27] Armstrong-Hélouvry, B., Dupont, P., and De Wit, C. C., "A Survey of Models, Analysis Tools and Compensation Methods for the Control of Machines with Friction, *Automatica*, Vol. 30, No. 7, 1994, pp. 1083-1138.
[28] Pitenis, A. A., Dowson, D., and Sawyer, W. G., "Leonardo da Vinci's Friction Experiments: An Old Story Acknowledged and Repeated," *Tribology Letters*, 56(3), 2014, pp. 509-515.
[29] Wagner, J. L., Beresh, S .J., Kearney, S. P., Trott, W. M., Castaneda, J. N., Pruett, B. O. and Baer, M. R., "A Multiphase Shock Tube for Shock Wave Interactions with Dense Particle Fields," *Experiments in Fluids*, Vol. 52, No. 6, 2012, pp.1507-1517.
[30] Wagner, J. L., DeMauro, E. P., Casper, K. M., Beresh, S. J., Lynch, K. P., and Pruett, B. O., "Pulse-Burst PIV of an Impulsively Started Cylinder in a Shock Tube for Re > 10^5, *Experiments in Fluids*, Vol. 59, No. 6, 2018, pp. 106.
[31] Mirels, H., "Shock Tube Test Time Limitation due to Turbulent Wall Boundary Layer," *AIAA Journal*, Vol. 2, No. 1, 1964, pp. 84-93.
[32] Egami, Y., Sato, Y., and Konishi, S., "Development of Polymer/Ceramic Pressure-Sensitive Paint with the same response time as Anodized-Aluminum PSP," AIAA Paper 2018-1032, January 2018.
[33] Gregory, J. W., Sakaue, H., Liu, T., and Sullivan, J. P., "Fast Pressure-Sensitive Paint for Flow and Acoustic Diagnostics, *Annual Review of Fluid Mechanics*, Vol. 46, 2014, pp. 303-330.
[34] Bell, J. H., and McLachlan, B. G., "Image Registration for Pressure-Sensitive Paint Applications," *Experiments in Fluids*, Vol. 22, No. 1, 1996, pp. 78-86.
[35] Venkatakrishnan, L., "Comparative Study of Different Pressure-Sensitive-Paint Image Registration Techniques, "AIAA Journal, Vol. 42, No. 11, 2004, pp. 2311-2319.
[36] Bell, J. H., Schairer, E. T., Hand, L. A., and Mehta, R. D., "Surface Pressure Measurements using Luminescent Coatings," *Annual Review of Fluid Mechanics*, Vol. 33, No. 1, 2001, pp. 155-206.
[37] Taira, K., Brunton, S. L., Dawson, S. T., Rowley, C. W., Colonius, T., McKeon, B. J., Schmidt, O. T., Gordeyev, S., Theofilis, V., and Ukeiley, L. S., 2017, "Modal Analysis of Fluid Flows: An Overview," *AIAA Journal*, 2017, pp. 4013-4041.